Ultramicroscopy 111 (2011) 1206–1213

Contents lists available at ScienceDirect

Ultramicroscopy

journal homepage: www.elsevier.com/locate/ultramic

High resolution surface morphology measurements using EBSD cross-correlation techniques and AFM

M.D. Vaudin *, G. Stan, Y.B. Gerbig, R.F. Cook

Ceramics Division, National Institute of Standards and Technology, Gaithersburg, MD 20899, USA

ARTICLE INFO

Article history:
Received 9 November 2010
Received in revised form
24 January 2011
Accepted 27 January 2011
Available online 3 February 2011

Keywords:
EBSD
Cross-correlation
AFM
Indentation

ABSTRACT

The surface morphology surrounding wedge indentations in (0 0 1) Si has been measured using electron backscattered diffraction (EBSD) and atomic force microscopy (AFM). EBSD measurement of the lattice displacement field relative to a strain-free reference location allowed the surface uplift to be measured by summation of lattice rotations about the indentation axis. AFM was used in intermittent contact mode to determine surface morphology. The height profiles across the indentations for the two techniques agreed within 1 nm. Elastic uplift theory is used to model the data.

Published by Elsevier B.V.

1. Introduction

The measurement of lattice strains and rotations with a precision of 10^{-4} and spatial resolution of 20 nm has become possible over the past few years [1]. Such measurements have been accomplished by comparing electron backscattered diffraction (EBSD) patterns using cross-correlation; the patterns are recorded in a scanning electron microscope (SEM). The technique has been applied to the measurement of strain accommodation in an austenite matrix around martensite inclusions in a ferrous alloy [2], investigation of strains and rotations on epitaxial $Si_{0.85}Ge_{0.15}$ mesas on silicon (Si) [3], and determination of localized deformation caused by nanoindentations in a steel polycrystal [4]. The technique was included in a recent review of miniaturized testing methods for metals and ceramics [5]. The term high resolution EBSD (HR-EBSD) has been coined to describe this method of comparing EBSD patterns (EBSPs) to measure relative lattice strains and rotations.

HR-EBSD was recently applied to analysis of the residual strain field surrounding wedge indentations in Si, and the computed stresses were compared with those measured using confocal Raman microscopy (CRM). Very good agreement between the EBSD and CRM measurements was obtained [6], thus validating that both methods were able to measure strains and stresses with nano-scale spatial resolution. In addition, the in-plane residual stress, σ_{xx}, normal to a wedge indentation aligned with the y-axis decreased as $x^{-1.9}$ (see Fig. 1(a) for the coordinate system used), very close to the x^{-2} dependence associated with the expansion of a cylinder in an infinite medium [7,8]. The residual stress field in the matrix adjacent to the contact impression in the Si was generated by a localized zone of plastically deformed and phase transformed material compressed by the indentation process and acting to expand against the restraining elastic matrix. On loading, the indenting wedge generated a zone of localized irreversible deformation beneath the contacted surface, as well as extended elastic deformation associated with the contact load *and* the strain mismatch between the irreversibly deformed zone and the surrounding constraining matrix. In Si, the irreversible deformation occurs by slip plasticity and phase transformation [9–11]. On unloading, the material recovered elastically as the contact load was removed, but the matrix retained the elastic deformation associated with the formation of the residual, irreversibly-deformed zone, which can be modeled as an embedded cylinder. An aspect of this deformation, and a consequence of the fact that the zone is not in an infinite medium but localized beneath the residual contact impression on a free surface, is that in acting to expand, the zone also generates surface uplift, u_z, adjacent to the contact impression.

It is this uplift that is the focus of the current work, continuing the use of wedge indentations in Si as test vehicles for deformation and strain measurement method development: EBSD techniques are extended into the area of morphology measurement using a single element of the displacement gradient tensor measured by EBSD, rather than the symmetric component of the full tensor used in strain measurement [1,6]. Here, EBSD is used to measure local lattice rotations, and atomic force microscopy (AFM) is used to

* Corresponding author.
E-mail address: mark.vaudin@nist.gov (M.D. Vaudin).

0304-3991/$ - see front matter Published by Elsevier B.V.
doi:10.1016/j.ultramic.2011.01.039

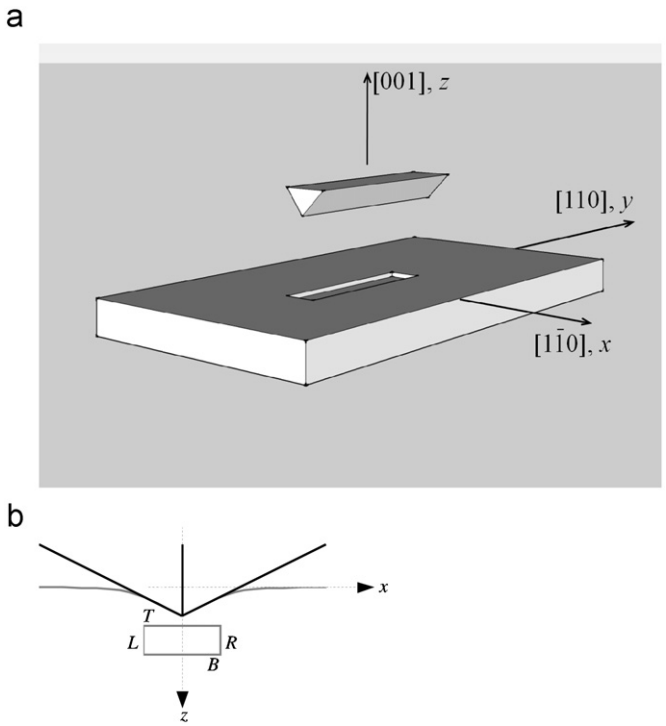

Fig. 1. Schematic diagrams of wedge indentation in a Si(0 0 1) surface: (a) coordinate system used in surface morphology measurements and analysis and (b) cross-section indicating the coordinates of the expanding cavity model used to describe the surface morphology.

measure height profiles surrounding wedge indentations in Si(0 0 1); the surface morphology deduced from both techniques is compared. It will be shown that these results provide a basis for traceability of EBSD cross-correlation technique measurements to the International System (SI) of units. The surface morphology is also compared with an expanding zone model for the surface uplift, providing insight into the nature of the sub-surface irreversibly deformed zone.

Earlier work using EBSD to measure lattice rotations employed Hough-transform-based techniques, of the type typically used in crystallographic mapping studies [12]. Using these methods, Kysar and Briant [13] measured angles over a range of 10° around a crack in a single crystal of Sn. Kysar et al. studied wedge indentations in single crystal face-centered cubic metals such as Cu and Al [14], and Ni [15], and found lattice rotations in the range from 25° to −25°. Wert studied rolled Al single crystals and found rotations typically in the 5° to −5° range [16] and Chen et al. [17] studied sheared Al bicrystals and observed misorientations as great as 13°. Recently, Gardner et al. in collaboration with Kysar and co-workers have applied cross-correlation methods to wedge indentations in single crystal Ni, where significant plastic deformation was obtained. Lattice strains up to 1% and rotations as large as 15° were measured, enabling the lower bound for the density of geometrically necessary dislocations to be determined [18].

The precision of the Hough-based angular measurements in these studies is not reported, but examination of the data indicates that it is $\approx 0.25^\circ$ at best. Brewer et al. [12] discussed mapping plastic deformation with EBSD and quoted the "standard angular resolution cited for EBSD as $\approx 0.5^\circ$ (≈ 0.01 rad)." In the current study, the plastically deformed region in the indented Si is localized to the contact region and the relationship between the elastic strain and rotation fields and surface uplift is investigated. Note that compared to the Hough transform-based method, the HR-EBSD cross-correlation technique used here and in [18] results in two orders of magnitude improvement in rotation resolution.

2. Material and experimental methods

2.1. Material and indentation procedure

The test sample was a $10 \times 20\ \text{mm}^2$ die cleaved from a semiconductor grade (0 0 1) Si wafer. In order to obtain decreased surface roughness essential for the AFM measurements the samples were not the same as those used previously for previous wedge indentation studies [6]. The sample was indented with a linear diamond wedge indenter, included angle of 140°, to a peak load of 350 mN at a loading and unloading rate of 10 mN/s, using an instrumented indenter in which the load and displacement were recorded during the contact event.

The long axis of the wedge was 20 μm in length and this axis was aligned along Si[1 1 0] during indentation. Five indentations, separated by 100 μm, were formed. In the center of the indentations the strain and rotation fields associated with the residual contact impressions were relatively unvarying parallel to the impression axes so that perpendicular line scans across the impressions performed by EBSD and AFM could be readily compared. A Cartesian coordinate system was used for the samples, with the z-axis normal to the sample (0 0 1) surface, the y-axis parallel to the [1 1 0] long axis of the contact impression, and the x-axis parallel to the line scans, see Fig. 1(a); the x-, y-, and z-axes are also designated as $\underline{x}_1$, $\underline{x}_2$, and $\underline{x}_3$, respectively.

2.2. AFM measurement method

AFM imaging to obtain height profiles was carried out using intermittent contact mode. The scan direction was aligned perpendicular to the indentation impressions in the x-direction. The scans were 1024×512 pixels (x by y) and covered an area $60 \times 15\ \mu\text{m}^2$. Representative scan profiles every 2 μm along the impression length were calculated by averaging the data from 0.5 μm strips (17 scan lines). The profiles within 5 μm of the center of the impression differed by less than 1 nm; this meant that the height profile in the x-direction was relatively unchanged over a substantial portion of the central part of the indentation, which significantly facilitated the morphological measurements and comparisions. Calibration of the AFM using an artefact of ultrasharp SiO_2 steps on a Si wafer showed that the AFM z measurements were accurate $\pm 4\%$ (one standard deviation)

2.3. EBSD measurement method

To record the EBSD measurements, each indentation was aligned with the y-axis of the SEM stage and a scan was performed in 250 nm steps across the center of the indentation in the x-direction, collecting high-quality EBSPs using the maximum resolution of the Oxford-HKL system [19] employed (1024×1344 pixels) and integration times of 1 s or more. The SEM (Hitachi 4700 FEGSEM) was typically operated at accelerating voltages from 10 to 30 kV and emission currents from 30 to 40 μA. The conditions used for the data presented here were an accelerating voltage of 20 kV, an emission current held between 30 μA and 35 μA, and a sample tilt of 70°; collection times were typically around 1 s per pattern. A pattern obtained from a strain-free point on the sample (denoted as the reference point, x_r) was chosen as the reference pattern and the other patterns were compared with this reference. The patterns were equally cropped from both sides to 1024×1024 pixels, and twenty 256×256 pixel regions of interest (ROIs) in each pattern were

cross-correlated. A ROI from a strained EBSP was cross-correlated with the same ROI from the reference pattern using Fourier methods. The displacement of the peak in the cross-correlation away from the center of the ROI provided the relative shift of the diffraction pattern at the center of the ROI.

The cross-correlation technique was routinely validated by scanning over a strain-free part of the Si sample. For these strain-free scans, the pattern center of each pattern (defined as the point on the detector nearest, where the electron beam impacts the sample) moves in synchrony with the beam impact position. Thus, the shift detected for all the ROIs in a specific EBSP is equal to the shift of the electron beam between where that pattern and the reference pattern were obtained. From a strain-free scan, plotting the average ROI shift for each pattern (in pixels) against the beam position (μm) and taking the inverse of the gradient gave the pixel size of the detector as 29.5 μm. From the pixel size and the movement of the electron beam, the ROI shifts induced by beam movement were calculated and subtracted from the measured shifts, and the displacement gradient tensor was calculated from the corrected ROI shifts. The EBSD data analysis carried out using the CrossCourt software package [20] uses this correction strategy. The strategy was validated by the fact that no significant rotation or strain was calculated during such strain-free scans. It was also determined that each ROI shift was measured with a standard deviation of between 0.05 and 0.1 pixels. As the distance from the sample to the detector is about 500 pixels (≈ 15 mm), the angular shift of the ROIs can be measured with a precision of 1×10^{-4}–2×10^{-4} rad which, combined with the oversampling inherent in using 20 ROIs, allowed rotations to be measured with a precision on the order of 5×10^{-5} rad. Calibration of the SEM using a prototype NIST SRM (2090) indicated that it was accurate in x to better than 1% (one standard deviations).

The analysis required the use of a reference pattern, which was typically one of the first four patterns obtained in a scan, and the level of strain at this point in the scan was below the detectability limit ($\approx 10^{-4}$). By using a reference pattern from the scan, the movement of the electron beam between the reference pattern and other patterns in the scan was well-defined, as discussed above with reference to the strain-free scans, thus minimizing the introduction of errors in the calculated strains. To explore ways to collect more data in a given time, patterns were collected with 512×512 pixel resolution and analyzed with 128×128 pixel ROIs. It was found that at this resolution, the uncertainties in stress and strain were approximately doubled, and the data collection time was approximately one third. Thus, reduced resolution data collection is potentially an option, particularly for strain mapping an area, where reduction of experimental time without significant degradation in data quality could be useful.

3. Analysis methods

3.1. EBSD analysis

The set of EBSPs collected during a scan across an indentation was analyzed to determine the complete displacement gradient tensor, $a_{ij}=\partial u_i/\partial x_j$, at each point in the scan, where the u_i is displacements in the $\underline{x}_i$ direction. It is possible to separate a_{ij} into symmetric and antisymmetric components:

$$\varepsilon_{ij}=(a_{ij}+a_{ji})/2,\qquad \omega_{ij}=(a_{ij}-a_{ji})/2 \tag{1}$$

where ε_{ij} is the strain as usually used in EBSD strain mapping [1,3,4,6]; if ε_{ij} is identically zero, ω_{ij} represents a rigid body rotation. Here we are interested in the orientation of the surface for $\varepsilon_{ij}\neq0$, although the maximum strains are small, ≈0.01 [6]. Under these conditions, if it is assumed that the reference plane of the Si sample at x_r is normal to $\underline{x}_3$, the angle in radians, measured in the x–z plane, between the reference plane and the sample surface at any other point along the electron beam scan, is given by the single displacement gradient tensor element $\partial u_3/\partial x_1=a_{31}$. As elastic strains of up to 1.5% were detected adjacent to the indent impressions, a more complete analysis was formulated for which the surface tilt angle was equal to $a_{31}(1-a_{11})$. This resulted in changes that were not significant compared to experimental uncertainty and so the simpler relation was used. EBSD is extremely surface sensitive; hence, measurements of lattice orientation provide local measurements of surface orientation. If it is assumed that prior to indentation the surface was flat, variation in surface orientation implies surface uplift; the assumption of flatness will be addressed below. AFM provides height data as a function of position on the sample, i.e., z as a function of x and y, and in particular for this case, u_3 as a function of x_1. To compare the surface morphologies deduced from the two techniques, either the variation in surface orientation or surface height must be compared; both comparisons have their merits. If the height of the surface at x_r (the reference pattern position) is taken as zero, the height, or uplift, u, at x is given by

$$u(x)=\int_{x_r}^{x}\frac{\partial u_3}{\partial x_1}dx_1 \tag{2}$$

such that an EBSD height profile across the indentation can be calculated. The step size, S, for the scan (250 nm) was sufficiently small that it could be assumed that the angle changed in a linear fashion between measured points and thus integration could be achieved by a simple summation without introducing a detectable error:

$$u(x)=\sum_{x_r}^{x}a_{31}\,S \tag{3}$$

It is assumed that there is no indentation-induced plasticity giving rise to discontinuities in the surface profile, outside of the indentation contact.

3.2. Wedge indentation analysis

The model used here to describe the height profile of the wedge indentation deformation field is based on the constrained dilatation of a thin rectangular prism of material located beneath the indentation contact. The prism is taken to be the irreversibly compressed zone of material generated by the contact that is acting to expand against the surrounding elastic matrix. The expression developed by Davies [21] for the normal displacement – the uplift – of an initially flat free surface under these conditions is

$$u_3(x)=\frac{(1+\nu)\varepsilon_0}{\pi}\left[(x-L)\ln\frac{(x-L)^2+B^2}{(x-L)^2+T}-(x-R)\ln\frac{(x-R)^2+B^2}{(x-R)^2+T^2}+2B\left(\tan^{-1}\frac{x-L}{B}-\tan^{-1}\frac{x-R}{B}\right)-2T\left(\tan^{-1}\frac{x-L}{T}-\tan^{-1}\frac{x-R}{B}\right)\right] \tag{4}$$

where L, R, T, B are the coordinates of the left, right, top, and bottom of the rectangular prism, respectively, as shown in Fig. 1(b), ε_0 is the characteristic linear strain imposed in the rectangle and is one third of the dilatation, and ν is Poisson's ratio of the material. T and B have opposite meanings from those used by Davies (as the problem is inverted). It is assumed here that as the indenting wedge was quite obtuse the perturbation of the indented surface from flatness at peak indentation load, when the irreversible zone reaches its greatest extent, does not influence the subsequent uplift. It is also assumed that, within the assumption of a rectangular deformation zone, the elastic

anisotropy of Si in the (1 1 0) deformation plane [22,23], does not significantly distort the uplift from that given by Eq. (4).

To fit the model of Eq. (4) to the experimental AFM data, $x=0$ was set in the height profile data as the lowest point of the residual contact impression as determined by AFM and the values of L and R were set as the AFM-measured contact impression edge locations, the highest points in the residual deformation field. Fitting was most easily accomplished by normalizing the height profile data and model predictions to one of these high points, $u_3(R)$. The model displacement at $x=R$ is given by

$$u_3(R) = \frac{(1+\nu)\varepsilon_0}{\pi}\left[(R-L)\ln\frac{(R-L)^2+B^2}{(R-L)^2+T^2} + 2B\tan^{-1}\frac{R-L}{B} - 2T\tan^{-1}\frac{R-L}{T}\right]$$
$$= \frac{(1+\nu)\varepsilon_0}{\pi}M \quad (5)$$

where for convenience the quantity in square brackets is designated M. With L and R fixed by the measured contact impression edge positions, the height profiles outside the contact impression were fit using Eq. (4), treating T and B as fitting parameters. The fitting procedure was manual adjustment of T and B to minimize the difference between the measurements and the model prediction over the domain $-20\ \mu m < L$ and $R < 20\ \mu m$. Knowledge of L, R, T, and B enabled M to be calculated, and thus the characteristic strain to be determined from the experimental value of $u_3(R)$ and inversion of Eq. (5):

$$\varepsilon_0 = \frac{\pi u_3(R)}{(1+\nu)M} \quad (7)$$

assuming an effective Poisson's ratio of $\nu=0.2$ (nu) in the Si(1 1 0) plane varies from 0.12 to 0.38 and in Si overall from 0.05 to 0.4 [22]; assuming a different effective value of ν within the rectangular zone assumption simply alters the inferred zone strain, ε_0.

The fit parameters also enabled the height profile inside the contact area to be predicted. At peak load, the contact depth, the depth over which the indenter contacts the surface, h_c, is given by

$$h_c = \frac{(R-L)}{2\tan\phi} \quad (8)$$

where $2\phi=140^\circ$ is the included angle of the indenter. At complete unload, the final impression depth, h_f, will be less than this due to the displacement inside the contact at $x=0$, $u_3(0)$, given by

$$u_3(0) = \frac{(1+\nu)\varepsilon_0}{\pi}\left[R\ln\frac{R^2+B^2}{R^2+T^2} - L\ln\frac{L^2+B^2}{L^2+T} + 2B\left(\tan^{-1}\frac{R}{B} - \tan^{-1}\frac{L}{B}\right)\right.$$
$$\left. -2T\left(\tan^{-1}\frac{R}{B} - \tan^{-1}\frac{L}{T}\right)\right] \quad (9)$$

superposed on the displacement outside the contact, $u_3(R)$, such that

$$h_f = -h_c + u_3(0) + u_3(R) \quad (10)$$

The residual profile inside the contact was assumed to consist of two linear segments from $u_3(L)$ to $h_f(0)$ to $u_3(R)$. Note that as L and R were assumed fixed from peak load to complete unload, this implies that the included angle of these line segments, $\phi_f > \phi$.

4. Results

Fig. 2 shows a typical load-displacement response obtained during 350 mN wedge indentation of Si(0 0 1); the response is similar to that observed during pyramidal or spherical indentation. The response is hysteretic with about 75% of the displacement recovered during unloading. During unloading there is a discrete pop-out at about 110 mN associated with transformation from Si-II phase to Si-III and Si-XII phases [9,24–26].

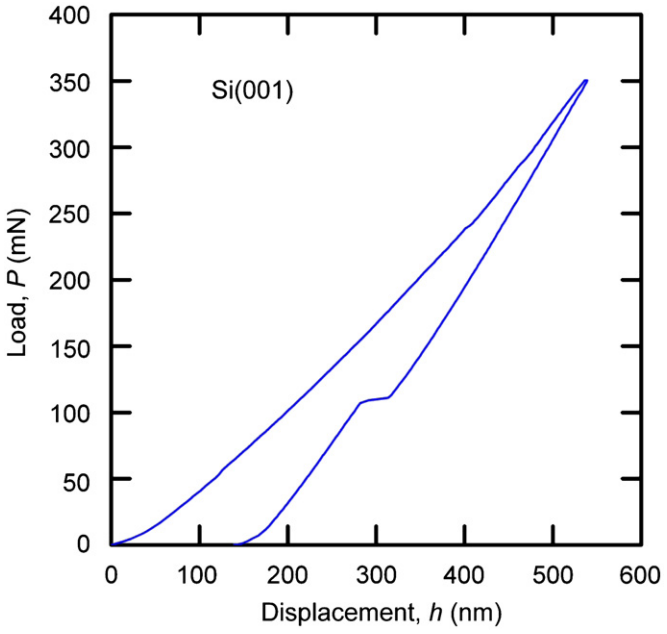

Fig. 2. Indentation load-displacement response during wedge indentation of Si(0 0 1).

The implication is that on loading, plastic deformation beneath the contact impression generated by dislocation motion on Si-I slip planes was limited by dislocation entanglement on intersecting slip planes [9,10] and subsequent indentation deformation was accommodated primarily by transformation of Si-I to Si-II. On unloading there was elastic recovery both internal and external to the contact area and final contact between the indenter and the surface was lost at an indentation depth of about 140–150 nm. The material associated with this residual contact impression depth was forced into a localized irreversible deformation zone consisting of plastically deformed and phase transformed material beneath the contact impression [9,10]. The load-displacement responses of all five indentations were similar.

Fig. 3 is an AFM image of a 350 mN wedge indentation, with a three dimensional inset showing the deep residual indentation impression, extending to about 90 nm below the surface in this case, and the significant uplift on either side of the impression, extending about 50 nm above the surface. A significantly elevated region extends approximately 10 μm to either side of the impression indentation, and it is this uplifted region that is of primary experimental interest in this work. Measurements of the AFM height profiles showed that the residual impression widths (the lateral distance between the highest points of the profile, R—L in the above notation) varied from 1.47 to 1.70 m and the net impression depths (the vertical distance $u_3(R)$—$u_3(0)$) varied from 129 to 151 nm, but were not correlated with the widths. The residual included angles (ϕ_f) varied from 154° to 150°. The maximum uplift ($u_3(R)$) varied considerably, from 36 to 90 nm. Close inspection of the inset of Fig. 3 shows that the impression is not symmetric in that the impression edge heights are not the same on the left and right, the residual impression faces make different angles with the sample surface, and the deepest extent of the impression is not centered between the impression edges. These features were common to all five indentations and are probably due to the diamond wedge being very slightly misaligned by an angle of the order of 1–3° such that the two faces of the wedge made different angles with the sample surface.

Fig. 4 is a plot of the three lattice rotations determined by EBSD, a_{12}, a_{23}, and a_{31}, which are rotations of the surface about

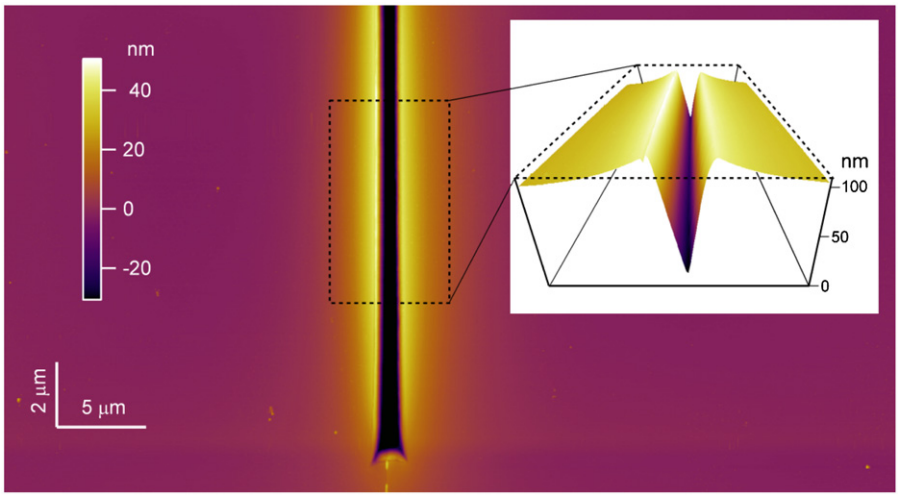

Fig. 3. AFM image of a wedge indentation in Si(0 0 1) showing the surface uplift adjacent to the residual contact impression.

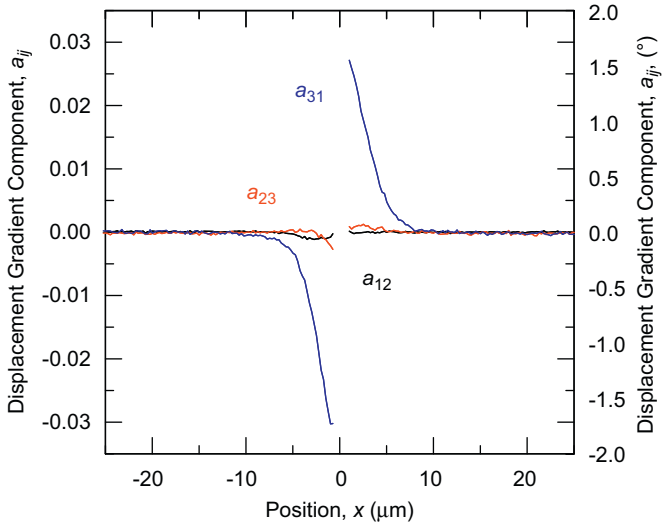

Fig. 4. Plot of lattice displacement gradient tensor components, a_{ij}, measured by EBSD, associated with residual deformation adjacent to a wedge indentation in Si(0 0 1).

the z-, x-, and y-axes, respectively. Only a_{31} has significant magnitude, with the other two rotations being at least an order of magnitude smaller. a_{31} is the rotation around the long axis of the indentation, and a_{31} rotations over 1.5° were measured immediately adjacent to the indentation. Fig. 5 shows plots of the height profiles for three indentations, determined by integration of EBSD data such as those in Fig. 4 using Eq. (3). These profiles are compared with profiles measured by AFM, setting the constant of integration such that the EBSD and AFM data agreed at a height of zero at position $x \approx -20$ μm. The profiles are exaggerated vertically by about a factor of 100. The very good agreement between the EBSD and AFM height profiles is clear—close to the indentation the maximum magnitude of the residual for Fig. 5(c) (*i.e.*, AFM height—EBSD height) is 2 nm, shown in the residual plot Fig. 5(d), and the root mean square of this residual is 0.76 nm. The residual behavior for all five indentations (two not shown) was similar. The AFM data indicated a small level of undulation on the sample surface of the order of 1 nm. AFM scans performed on a region of the Si well away from the indentations where the crystallographic orientation was unchanging showed height undulations of as much as 1.3 nm peak-to-valley with peak-to-peak separations of the order

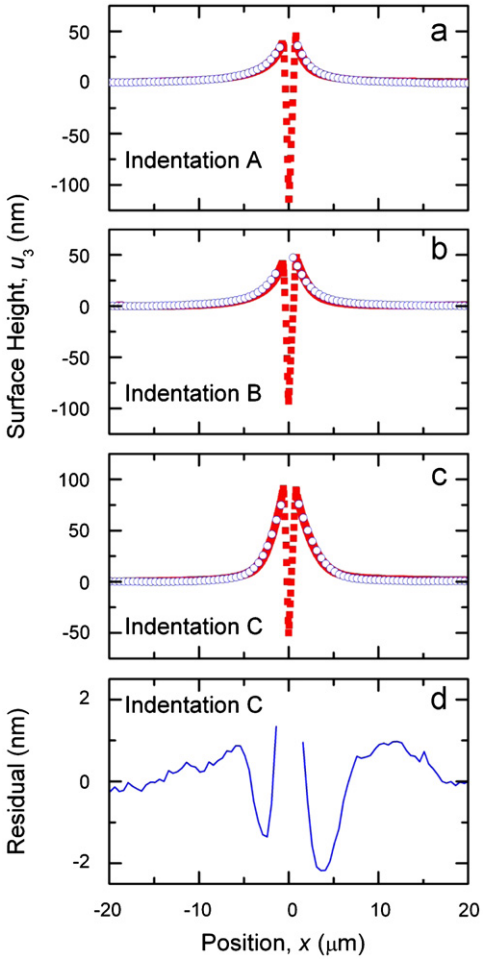

Fig. 5. (a)–(c) Plots of height profile comparisons obtained by AFM and EBSD for three wedge indentations in Si(0 0 1) and (d) plot of the residual difference between the height profiles obtained by AFM and EBSD for the wedge indentation data of (c).

20 μm. The EBSD height plot does not indicate these undulations as they are not accompanied by a change in crystallographic orientation. Thus, 10 μm or more from the indentation the residual is primarily caused by the surface undulation of the Si. Fig. 5 highlights the variability noted above in the impression edge heights and the consistency of the net impression depth.

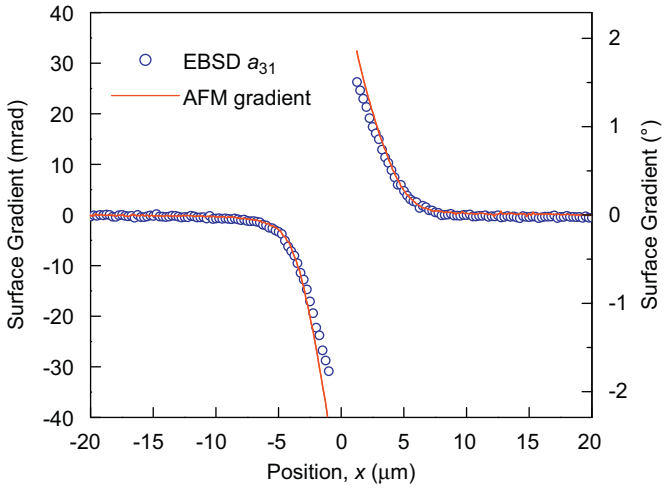

Fig. 6. Plots of the surface height gradient and lattice gradient obtained by AFM and EBSD, respectively, adjacent to a wedge indentation in Si(0 0 1); data correspond to the height profile in Fig. 5(c).

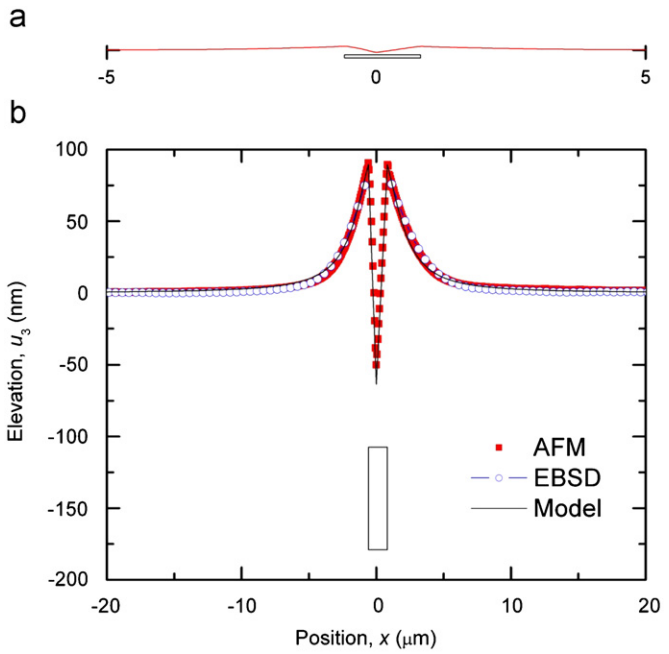

Fig. 7. Plots of experimental AFM and EBSD and fitted expanding-cavity model height profiles for the wedge indentation in Si(0 0 1) plotted in Fig. 5(c): (a) 10 μm wide AFM height profile of the indentation and the rectangular cavity and (b) 40 μm wide AFM and EBSD height profiles and the fitted model along with the position of the cavity (exaggerated vertically about 100 times).

The comparison of EBSD and AFM data required that height offsets of up to 4 nm between the two data sets were removed. Ideally, the AFM data would tend to a uniform height at the edges of the scan, but as discussed there were undulations of up to 1.3 nm in the wafer surface height, making it difficult to set a zero AFM height. Also, zero rotation for EBSD could not be established to be better than 10^{-4} rad. Eq. (3) shows that any error in a_{31} or S produces an error in the EBSD-measured height, $u(x)$. A constant error, δa, in a_{31} persisting over a scan of length D produces an error in $u(x)$ of $D\delta a$; this amounts to 2 nm over a 20 μm scan. In an alternative approach to data comparison that avoids the necessity of establishing zero height, the AFM data were differentiated to give the slope $\partial u_3/\partial x_1$, which was directly compared with a_{31} from EBSD. The raw AFM data were somewhat noisy and were smoothed over 9 data points (equivalent to 0.53 μm) before calculating the gradient from adjacent heights. Fig. 6 shows the slope comparison for the same indentation as Fig. 5(c). Clearly, the slopes agree very well; a small deviation only becomes apparent within 1 or 2 μm from the indentation edge. Errors in S, which are caused by SEM calibration errors, are a simple multiplicative factor for both the x- and z-axes, so that the EBSD-measured height profile is equally affected in x and z.

Fig. 7 shows a fit of the expanding prism model to the experimental observations for the indentation shown in Fig. 5(c). In Fig. 7(a), a 10 μm AFM scan across the indentation deformation field is shown at the real height to width aspect ratio of the field; the obtuse nature of the residual contact impression is apparent. In Fig. 7(b) the scan data from Fig. 5(c) are reproduced with the height exaggerated by about a factor of 100 as before. The solid line is a fit to the data; the model is clearly able to describe the observed profile both outside (where it was fit, Eq. (4)) and inside (where it was predicted, Eq. (10)) the contact impression. Also shown in both Fig. 7(a) and (b) is the location of the rectangular prism representing the compressed zone of material acting against the constraint of the surrounding matrix and giving rise to the uplift. The thin, surface-localized nature of this zone is made clear in Fig. 7(a). Note that the asymmetric location of the zone relative to the deepest point of the residual impression enables the asymmetric impression faces to be described.

The value of M for the model fit in Fig. 7 was $M=1.165$ μm, which, combined with the measured value of $u_3(R)=89.5$ nm, gives $\varepsilon_0=0.20$ from Eq. (7). Fits (not shown) to the data for the indentations in Fig. 5(a) and (b) were similar and gave $\varepsilon_0=0.056$ and 0.060, respectively. The smaller values of the characteristic strains for these indentations are consistent with the observation that the peak uplifts for these indentations (A and B) were smaller than that for the indentation C, although the net impression depths were similar.

5. Discussion

Microscopies based on two completely different physical principles – diffraction and profilometry – exhibited agreement for surface height and surface orientation measurements within experimental uncertainty, about 2 nm height and 0.1 mrad, respectively, in absolute terms. The test structure was a wedge indentation in a Si surface. The topography and orientation variations associated with the indentation elastic–plastic deformation field were approximately 150 nm and 25 mrad, respectively, indicating agreement between the two methods in relative terms of approximately 1%. This agreement, between SEM-based EBSD measurements and AFM-based profilometry measurements, is similar to that observed, on the same test structure, between EBSD and a microscopy based on yet another physical principle – Raman spectroscopy – of the stress and strain state adjacent to the indentation impression [6]. Agreement in that case, between EBSD and CRM, was to within about 10 MPa out of a field variation of over 1 GPa, again within about 1% in relative terms. The results here further confirm that EBSD deformation measurements, which can be broken down into strain, rotation, or orientation, provide both precise and accurate measurements. EBSD angular uncertainties of better than 10^{-4} were demonstrated here, two orders of magnitude greater precision than obtained using Hough transform methods [12–16].

The precision of the cross-correlation method could potentially be improved by a number of steps. The orientation of the detector may have small deviations from the assumed orientation, including tilt about the detector x- and y-axes and rotation

about the detector normal; these could be determined and corrections could be applied. The phosphor screens used for recording of the EBSPs typically have a granular microstructure, which imparts a weak background to the observed patterns and causes a small diminution in pattern shifts measured by cross-correlation. Background subtraction cannot completely eliminate this effect and it is therefore desirable to employ phosphors with minimal observable effect on the diffraction patterns. It has been shown [27] that barrel distortion by the lens that transfers the EBSP image from the phosphor to the recording chip can introduce detectable errors in measured strain values; this area would repay some attention. Finally, the diffraction pattern processing parameters – mainly the filter settings – are known to affect the pattern shifts and therefore the measured displacement gradient tensor.

The agreement between the EBSD and AFM measurements suggests the possibility of SI-traceable EBSD deformation measurements through a metrological link between SI-verifiable AFM measurements of surface morphology and lattice distortion measurements based on EBSD cross-correlation methods, and hence the establishment of the accuracy of EBSD measurements. Calibration of AFM measurements through the use of step height and pitch artifacts traceable to the SI unit of the m via the use of metrological AFMs and the wavelength of light [28] and calibration of the SEM through the use of NIST Reference Material 8820 (Scanning Electron Microscope Scale Calibration Artifact) could lead to SI-traceable deformation, strain, or rotation or relative orientation EBSD measurements. The accuracy of EBSD measurements could then be established in one of two ways: in the first way, both techniques could be applied to the sample of interest and the surface orientation related elements of the deformation gradient tensor calibrated via the AFM measurements. This would then ensure that sample strains or rotations determined from those elements were accurate, at least to within the measurement precision, and that bounds could be placed on sample strains and rotations determined with other elements using strain compatibility conditions and measurement precision. Not every sample would be amenable to this method. A more broadly-applicable second method is to apply both techniques to a test structure such that as many elements of the displacement gradient tensor as possible determined by EBSD were calibrated from the AFM measurements. EBSD could then be applied to an unknown sample with the measurement accuracy thence set by the transfer uncertainty from the AFM to the EBSD. The EBSD technique could itself be used as a transfer method to establish accuracy of CRM strain and stress measurements via the transfer chain of AFM–EBSD–CRM.

The wedge indentation in Si exhibits a very simple deformation state and remains a good candidate multi-purpose test structure: it simultaneously exhibits plane strain, $\varepsilon_{yy}=\varepsilon_{yx}=\varepsilon_{yz}=0$, as measurements can be performed near the center of a long, y-aligned, indentation contact impression, and plane stress, $\sigma_{zz}=\sigma_{zx}=\sigma_{zy}=0$, as the measurements can be localized to a z-normal surface [6]. An aspect of using a wedge indentation as the test structure in either of the traceability methods described above that was not addressed here is fixing the relative in-plane position and orientation. Here the EBSD x-direction scans were performed within a 0.5 μm wide stripe within which the AFM profiles were averaged in the y direction. In addition, the relative x positions of the measured or inferred profiles were set by matching the profiles around the center of the indentation. Finally, the relative z positions of the profiles were set by enforcing matching of the profiles a long way from the indentation. In order to generate truly SI-traceable EBSD and CRM measurements these degrees of freedom would have to be minimized, although comparison of profile derivatives (Fig. 6) obviates the need for an absolute z value. Minimizing these degrees of freedom would require the use of secondary features to fix the absolute location of the scans to be carried out by the two microscopy techniques; other small features on the Si surface would be suitable, say point indentations or lithographically patterned marks.

The expanding embedded rectangular prism model used here was well able to describe the surface topography both exterior and interior to the contact impression. The model is physically more consistent with the measured system than that of an expanding cylinder in an infinite medium as it explicitly takes the free surface into account and is thus able to predict surface uplift. The model provided insight into the nature of the subsurface deformation zone depth and characteristic strain, and the values obtained were consistent with previous measurements and predictions for hard materials: zone depths two to three times larger than impression depths and strains of order tens of percent [10,29]. The model provides yet another method of comparing and mutually calibrating the various microscopy techniques. AFM measurements of indentation height profile fields could be fit by the model to obtain the deformation zone parameters. These parameters could then be used in equations similar to Eq. 4 to predict the orientation, rotation, and strain fields adjacent to the residual impression for comparison with EBSD and CRM measurements.

Generation of internally calibrated deformation and strain fields from model predictions will require model refinement; however, at least for indentation test structures, in two ways. The first is concerned with the geometry of the misfitting expanding zone. The rectangular prism model is well suited to planar structures formed by lithography, in which the zone cross-section is close to rectangular: electron-beam-induced densified oxides [30], doped quantum well structures [31], or shallow trench isolation structures [32], and these would all be suitable AFM–EBSD–CRM calibration vehicles. Although obtuse indentations generate surface-localized deformation zones, the geometry is probably semi-elliptical in cross section [10]. Calculations similar to those applied to hemispherical indentation fields, correcting a spherical zone field in an infinite medium via Mindlin stress field techniques to generate a normal-traction-free plane to represent the free surface [33], or for various nuclei of strain in a semi-finite solid, that explicitly account for the free surface from the outset [34], could be used to generate models of the indentation field that better capture the semi-elliptical zone shape. However, to be truly useful as microscopy calibration tools any of these models must be refined in a second way to include the elastic anisotropy of the crystal. There is also a philosophical point here: EBSD and CRM both rely on crystalline anisotropy to determine strain, and hence models of strain in test structures, whatever the misfit zone shape, should take crystalline anisotropy into account.

Finally, a comment on the nature of the indentation uplift field is in order. Uplift or elastic recovery inside the indentation contact zone has been known since the earliest studies of hardness testing [35–38], although the focus on indentation of metals led to the idea that there was little or no elastic deformation exterior to the contact and therefore no exterior recovery—for example see Fig. 1 in [33], which did consider exterior recovery, and Fig. 8 in [33]. Even studies of indentation recovery in brittle materials that were well aware of the existence and effects of the localized indentation plastic deformation zone ignored exterior elastic deformation during and after contact – the diagram in [39] is essentially the same as that of Fig. 1 in [33] – as most attention was focused on the effects of the in-plane stress field on indentation cracking [25]. The concomitant out-of-plane displacement was not considered although it was recognized as

existing—for example see the diagram in [25]. Residual uplift exterior to the contact was associated with the extended plastic deformation zones prevalent in metals [32] and the extrusion of plastically deformed material from beneath the contact to the surface [31], although the idea has also been used to explain exterior uplift in brittle materials such as MgO crystals [40] and bulk metallic glass [41]. The view here for brittle materials is very different and considers the plastic deformation zone to be localized beneath the contact such that, in addition to exterior recovery due to unloading, there is exterior uplift in reaction to the plastic deformation zone formation. In this regard, it is notable that the AFM cross-section of the indentation in the bulk metallic glass [37] is extremely similar to that of Fig. 5, with very well-defined impression edges suggestive of plastic deformation localized beneath the contact. Interpretation of the cross-section of the MgO indentation [36] is less clear, but there is similarity with Fig. 5 in that there are clear surface tilts some distance from the contact impression. The observations suggest that exterior uplift in these two cases may well be elastic and not plastic deformation.

6. Conclusions

Microscopies based on two completely different physical principles have been applied to the analysis of the uplift surrounding wedge indentations in silicon. A technique based on electron diffraction and conducted in the SEM, HR-EBSD, and a scanned probe microscopy, AFM, were both used to measure uplift profiles across the wedge indentation impression. Comparisons were made between (1) the integral (or summation) of the EBSD-measured rotation profile and the AFM-measured height, and (2) the EBSD displacement gradient tensor and the derivative of the AFM height field. The results showed excellent quantitative agreement in both cases. For example, considering comparison (1), the residual Fig. 5(d) had a root mean square value of 0.76 nm. The work confirmed the ability of EBSD cross-correlation methods to determine displacement gradient tensor coefficients with a precision of 10^{-4}. Modeling of the profiles across the indentation impressions, following the work of Davies [19], was applied very successfully to the profiles both outside the indentation impression, where AFM provided experimental data to which the model could be fit, and inside, where the model predictions derived from the outside fit matched very well with the AFMThe potential use of AFM to establish SI traceability for EBSD and CRM measurements was discussed and this will provide the basis for further work in this area. observations, even down to the asymmetries observed in the profiles.

References

[1] A.J. Wilkinson, G. Meaden, D.J. Dingley, Ultramicroscopy 106 (2006) 307.
[2] G. Miyamoto, A. Shibata, T. Maki, T. Furuhara, Acta Mater. 57 (4) (2009) 1120.
[3] A.J. Wilkinson, Appl. Phys. Lett. 89 (2006) 241910.
[4] A.J. Wilkinson, D. Randman, Philos. Magn. 90 (9) (2010) 1159.
[5] J.D. Lord, B. Roebuck, R. Morrell, T. Lube, Mater. Sci. Technol. 26 (2) (2010) 127.
[6] M.D. Vaudin, Y.B. Gerbig, S.J. Stranick, R.F. Cook, Appl. Phys. Lett. 93 (2008) 193116.
[7] R. Hill, The Mathematical Theory of Plasticity, Oxford University Press, Oxford, 1986.
[8] B.L. Symonds, R.F. Cook, B.R. Lawn, J. Mater. Sci. 18 (1983) 1306.
[9] J.E. Bradby, J.S. Williams, J. Wong-Leung, M.V. Swain, P. Munroe, J. Mater. Res. 16 (2001) 1500.
[10] J. Zarudi, L.C. Zou, Zhang, Appl. Phys. Lett. 82 (2003) 874.
[11] A.J. Haq, P.R. Munroe, J. Mater. Res. 24 (2009) 1967.
[12] A.J. Schwartz, M. Kumar, B.L. Adams, D.P. Field (Eds.), Electron Backscatter Diffraction in Materials Science, 2nd edn., Kluwer Academic, New York, 2009.
[13] J.W. Kysar, C.L. Briant, Acta Mater. 50 (2002) 2367.
[14] J.W. Kysar, Y.X. Gan, T.L. Morse, X. Chen, M.E. Jones, J. Mech. Phys. Solids 55 (2007) 1554.
[15] J.W. Kysar, Y. Saito, M.S. Oztop, D. Lee, W.T. Huh, Int. J. Plasticity 26 (2010) 1097–1123.
[16] J.A. Wert, Acta Mater. 50 (2002) 3125.
[17] D. Chen, J.-C. Kuo, S.-H. Tung, M.-H. Shih, Mater. Sci. Eng. A. 454-455 (2007) 523.
[18] C.J. Gardner, J. Kacher, J. Basinger, B.L. Adams, M.S. Oztop, J.W. Kysar, Experimental Mechanics, doi:10.1007/s11340-010-9441-4.
[19] Certain commercial equipment, instruments or materials are identified in this paper to adequately specify the experimental procedure. Such identification does not imply recommendation or endorsement by the National Institute of Standards and Technology, nor does it imply that the materials or equipment identified are necessarily the best available for the purpose.
[20] A.J. Wilkinson, G. Meaden, D.J. Dingley, Mater. Sci. Technol. 22 (2006) 1271.
[21] J.H. Davies, J. Appl. Mech. 70 (2003) 665.
[22] Wortman and Evans, Ultramicroscopy, this issue.
[23] Brantley, Ultramicroscopy, this issue.
[24] V. Domnich, Y. Gogotsi, S. Dub, Appl. Phys. Lett. 76 (2000) 2214.
[25] J. Jang, M.J. Lance, S. Wen, T.Y. Tsui, G.M. Pharr, Acta Mater. (2005) 1759.
[26] Y.B. Gerbig, S.J. Stranick, D.J. Morris, M.D. Vaudin, R.F. Cook, J. Mater. Res. 24 (2009) 1172.
[27] T.B. Britton, C. Maurice, R. Fortunier, J.H. Driver, A.P. Day, G. Meaden, D.J. Dingley, K. Mingard, A.J. Wilkinson, Ultramicroscopy, in press.
[28] R.G. Dixson, N. Orji, J.E. Potzick, M.W. Cresswell, R.A. Allen, S.J. Smith, A.J. Walton, Proc. SPIE 6730 (2007) 67303D.
[29] S.S. Chiang, D.B. Marshall, A.G. Evans, J. Appl. Phys. 53 (1) (1982) 298.
[30] S. Garcia Blanco, A. Glidle, J.H. Davies, J.S. Atchison,and, J.M. Cooper, Appl. Phys. Lett. 79 (2001) 2889.
[31] J.H. Davies, D.M. Bruls, J.W.A.M. Vugs, P.M. Koenraad, J. Appl. Phys. 91 (2002) 4171.
[32] C.E. Murray, M. Sankarapandian, S.M. Polvino, I.C. Noyan, B. Lai, Z. Cai, Appl. Phys. Lett. 90 (2007) 171919.
[33] S.S. Chiang, Ph.D. Thesis, University of California, Berkeley, 1981.
[34] R.D. Mindlin, D.H. Cheng, J. Appl. Phys. 21 (1950) 926.
[35] D. Tabor, The Hardness of Metals, Clarendon Press, Oxford, 1951.
[36] T.O. Mulhearn, J. Mech. Phys. Solids 7 (1959) 85.
[37] N.A. Stillwell, D. Tabor, Proc.Phy. Soc. Lond. 78 (1961) 169.
[38] D.M. Marsh, Proc. R. Soc. A. 279 (1964) 420.
[39] B.R. Lawn, V.R. Howes, J. Mater. Sci 16 (1981) 2745.
[40] K. Sangwal, P. Gorostiza, J. Servat, F. Sanz, J. Mater. Res. 14 (10) (1999) 3973.
[41] K. Ai, L.H. Dai, Scri. Mater. 56 (2007) 761.